PERGAMON

International Journal of Solids and Structures 37 (2000) 6843–6867

INTERNATIONAL JOURNAL OF SOLIDS and STRUCTURES

www.elsevier.com/locate/ijsolstr

On the dynamics of propagating buckles in pipelines

S. Kyriakides *, T.A. Netto

Research Center for Mechanics of Solids, Structures and Materials, WRW 110, The University of Texas at Austin, Austin, TX 78712-1085, USA

Received 10 November 1999

Dedicated to the memory of Warner T. Koiter

Abstract

A combined experimental and analytical study of the dynamic propagation of buckles initiated in long pipes under external pressure is presented. The experiments involve measurement of the steady-state velocity of buckles initiated in stainless steel tubes with $D/t = 27.9$. Results from tubes pressurized by air or water are presented for pressure levels ranging from the propagation pressure to the collapse pressure of the tube. The buckle velocity in air was found to be significantly higher than in water at the same pressure. The flip–flop mode of buckle propagation was found to take place for pressure levels 13% below the collapse pressure and higher.

A finite element model, capable of simulating the dynamic initiation and propagation of such buckles has been developed. The model accounts for the inertia of the pipe, the nonlinearity introduced by contact between the collapsing walls of the pipe while the material is modeled as a finitely deforming elastic–viscoplastic solid. The buckling and collapse are assumed to take place in vacuum. The model is shown to reproduce well the dynamic initiation and propagation of buckles in air and the predicted velocities are in good agreement with those measured in this medium. The buckle was found to sharpen significantly with pressure. This sharpening, coupled with higher pressure, causes an increase in the amplitude of reverse ovality in a zone just ahead of the propagating buckle front. At higher pressures, the reverse ovality is shown to be high enough to initiate collapse at a new site. The new collapse is at 90° to the original one. This sequence of events is repeated, resulting in the flip–flop mode of buckle propagation.

Keywords: Propagating buckles; Pipelines; Dynamic buckling; Flip–flop mode

1. Introduction

Buckling and collapse due to external pressure are important issues governing the design of pipelines installed in deep waters. A second concern, often of equal importance, is the survival of the line in case a propagating buckle is accidentally initiated in the pipeline. Propagating buckles can be initiated from a locally weakened section of the pipe for instance due to a dent induced by impact by a foreign object (Kyriakides et al., 1984a; Park and Kyriakides, 1996), due to a local buckle resulting from excessive

* Corresponding author. Fax: +1-512-471-5500.
E-mail address: skk@mail.utexas.edu (S. Kyriakides).

0020-7683/00/$ - see front matter
PII: S0020-7683(99)00317-0

bending during installation (Johns et al., 1975; Murphey and Langner, 1985; Corona and Kyriakides, 1988; Ju and Kyriakides, 1991) or due to a wall thickness reduction caused by wear or corrosion. Once initiated, buckles propagate at high velocities and have the potential of quickly destroying the whole line. The lowest pressure at which such a buckle propagates is the *propagation pressure* (P_P), a characteristic pressure of the pipe (Kyriakides and Babcock, 1981; Dyau and Kyriakides, 1993b). The propagation pressure is typically only 15–20% of the *collapse pressure* (P_{CO}) and so in most projects, designing the line based on the propagation pressure is impractical. The preferred alternative is to base the design on the collapse pressure and install buckle arrestors at regular intervals along the length of the line. In the event of initiation of a buckle, the arrestors limit the damage to the length of pipe separating the arrestors on either side of the initiation site (typically a few hundred feet).

Buckles initiated at any pressure higher than P_P propagate dynamically. Velocities of hundreds of feet per second were reported by Kyriakides and Babcock (1979) in experiments on model aluminum tubes (the measured velocities were reproduced by a numerical model by Song and Tassoulas, 1993). Even higher velocities were recently reported from similar experiments on stainless steel tubes (Netto and Kyriakides, 2000a). In both studies, it was shown that buckle velocities in experiments in which air was the pressurizing fluid were significantly higher than buckle velocities at the same pressure in water. This confirms that the velocity of propagation is influenced by an interaction between the collapsing structure and the pressurizing fluid (see. Netto et al., 1999).

To date, most work on buckle propagation in pipelines has dealt with the issues of initiation of propagating buckles from local buckles and dents (e.g. Kyriakides et al., 1984b; Dyau and Kyriakides, 1993a; Park and Kyriakides, 1996), and with the prediction of the propagation pressure (see Chater and Hutchinson, 1984 and the review in Kyriakides, 1993). These problems are dealt with adequately at the quasi-static setting. By contrast, the dynamics of propagating buckles have received less attention. Dynamic buckle propagation differs from quasi-static propagation in several ways which influence the final collapsed state. For example, the inertial loads contribute to the deformation of the collapsed pipe and increase the potential of cracking of the highly strained pipe wall; the dynamic engagement of arrestors by running buckles alters their arresting performance (Kyriakides and Babcock, 1980; Netto and Kyriakides, 2000a,b); the high strain rates that are induced by dynamic collapse to parts of the collapsing walls may alter the collapse profile; influence of dynamics on both pipe girth and seam welds is also an issue of practical concern. An additional issue, perhaps of more scientific rather than practical interest, is the *flip–flop* mode of buckle propagation discovered in the experiments of Kyriakides, 20 years ago (Kyriakides and Babcock, 1979; Kyriakides, 1980).

Netto and Kyriakides (2000a) recently reported some new results on the dynamics of propagating buckles obtained in the course of a study of the dynamic performance of integral buckle arrestors. They include measurements of steady-state buckle velocities in air and water for a specific range of pressures. The experiments were conducted on stainless steel (SS) 304 seamless tubes with $D/t = 27.9$ (nominal). Dynamic experiments in air were simulated numerically with success. The simulations revealed the mechanism through which dynamics enhances the performance of such arrestors. In the present article, we extend the testing pressures to cover the whole range of interest ($P_P < P < P_{CO}$) and use the numerical model developed to study dynamic buckle propagation in more detail.

2. Experiments

2.1. Experimental setup and procedure

The objective of the experiments is to initiate a propagating buckle in a long tube in a constant pressure environment, let it accelerate to steady-state and measure its velocity. This is done for several values of

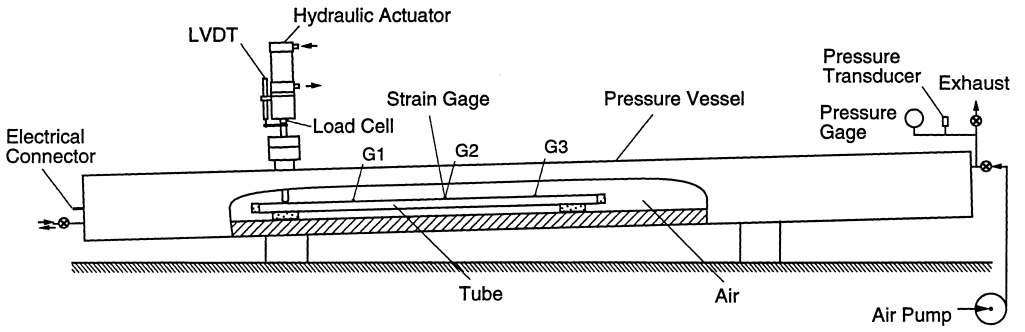

Fig. 1. Schematic of experimental setup used in dynamic buckle propagation experiments.

pressure in the range $P_P < P < P_{CO}$. The methodology followed is similar to that used by Kyriakides (1980) but the experiments were conducted in a larger testing facility with a much higher pressure capacity. Fig. 1 shows the testing setup used. The main component is a 7 in. (178 mm) internal diameter, 13 ft (4 m) long pressure vessel with a pressure capacity of 9000 psi (620 bar). It can be pressurized by water or air.

The test specimens are seamless SS-304 tubes with a diameter of 1.75 in. (44.5 mm) and a nominal wall thickness of 0.065 in. (1.65 mm). The length of the test specimens in the majority of the dynamic tests was 32 tube diameters. Three strain gages $(G_i, i = 1, 3)$ are mounted along the length of the tube (Fig. 1) for the purpose of establishing the velocity at which the buckle propagates. The strain gages and the connecting cables are covered with a compliant coating for water proofing. Each tube is sealed with solid end plugs, and the assembly is placed in the vessel so that its axis is at a level of one-third of the vessel inner diameter from the lowest point of the vessel inner wall as shown in Fig. 2.

When water is the pressurizing fluid, the vessel is filled with water leaving an air pocket which is then pressurized by air using air boosters. The size of the air pocket is large enough so that the pressure drop after the tube collapses is approximately 5% or less of the initial value. For air experiments, the vessel is directly pressurized by air.

Once the desired pressure is reached, a buckle is initiated close to one end of the tube by impact with a circular steel indentor shown in Fig. 2. The indentor is connected to a hydraulic actuator external to the vessel which is mounted onto the loading frame shown in the figure. A load cell and an LVDT displacement transducer are used to monitor the applied load and indentor displacement. The actuator is operated via a closed-loop servo controlled system shown schematically in Fig. 2. In these experiments, the actuator is operated under displacement control and the tube is impacted at a velocity of 0.5 in./s (12.7 mm/s).

The pressure is monitored by an electrical pressure transducer as well as by analog pressure gages. The pressure transducer signal, that of the load cell, the LVDT and the ones from the three strain gages, suitably conditioned, are monitored via a computer operated data acquisition system using the LabVIEW software. Typically, data are acquired at a rate of 50,000 sets of samples per second. The data acquisition system is triggered by the signal from the first strain gage but, by employing a pre-trigger feature of the system, data could be acquired from the moment the indentor motion commenced.

Fig. 3(a) shows a typical force history from the indentor and Fig. 3(b) shows the signals from the three strain gages all on a common time base (time zero is chosen arbitrarily). In this case, the ambient pressure was set at 1555 psi (107.2 bar) ($P_{CO} \approx 2184$ psi (150.6 bar)) and the pressurizing fluid was water. The indentor force is seen to increase up to a time of approximately 65 ms. We consider the load maximum to correspond to the initiation of local collapse (at 64.49 ms). The buckle requires some time to accelerate to steady-state propagation. Thus, it reaches G1 at 190.82 ms, G2 at 192.16 ms and G3 at 193.46 ms (negative

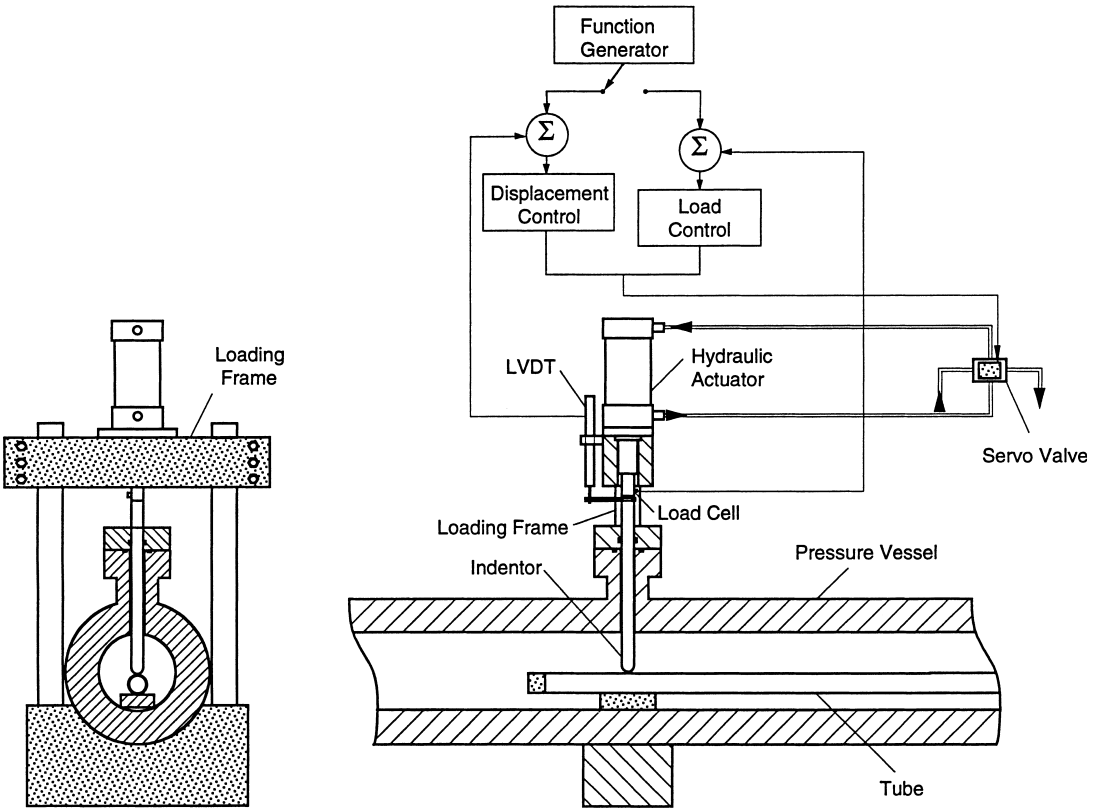

Fig. 2. Indentor and actuator used to initiate propagating buckles in tubes under external pressure.

voltage spikes). Using the distances between the gages, the velocity between G1 and G2 is evaluated to be 653 ft/s (199 m/s), and between G2 and G3 as 673 ft/s (202 m/s). We take the latter value to be the steady-state velocity. The strain gages were usually located at the top of the cross-section of the collapsing tube where they were oriented along the axial direction (see inset in Fig. 3(b)). The buckle profile involves a change in the sign of the local curvature and this is reflected in the signals.

2.2. Experimental results

2.2.1. Buckle velocity

Steady-state velocities (U) from eight experiments in air and 22 in water are plotted in Fig. 4 against the external pressure (*initiation pressure* P_I is the average of the pressure at the start and at the end of the test). The velocity is normalized by $\sqrt{\sigma_0/\rho}$, where σ_0 is the yield stress of the tube material measured in tensile tests on axial test coupons extracted from each tube used in the experiments and ρ is the steel density (0.280 lb/in.^{3} to 7750 kg/m^3). The pressure is normalized by the propagation pressure of each individual tube estimated by the following empirical relationship:

$$\hat{P}_P \approx \sigma_0 A \left(\frac{t}{D}\right)^{\beta}, \tag{1}$$

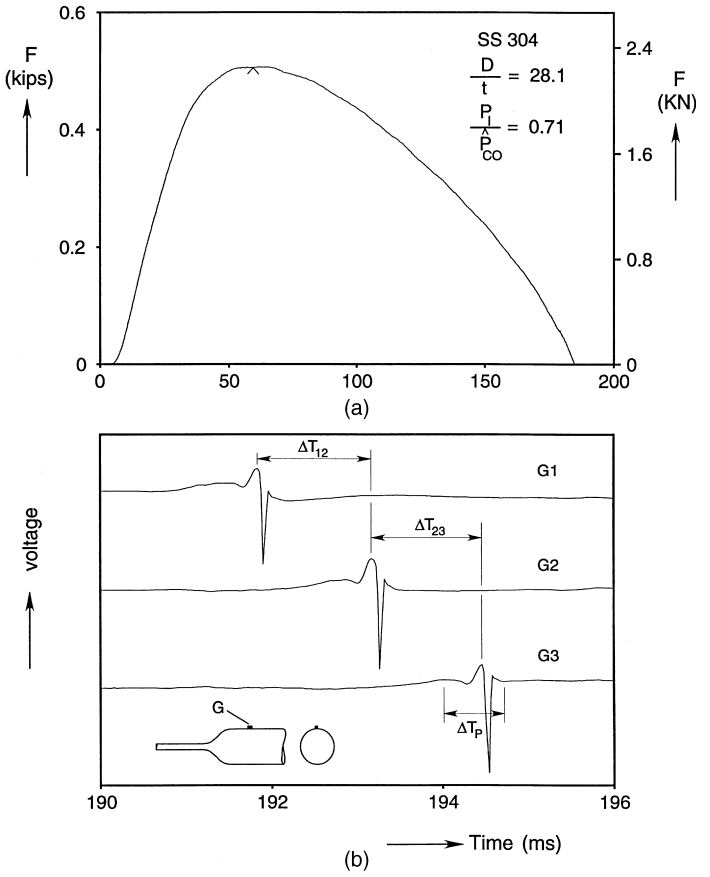

Fig. 3. Typical data recorded in a dynamic experiment: (a) indentor force and (b) strain gage signals as a function of time.

where D is the tube diameter and t, its wall thickness. For stainless steel, 304 $A = 35.547$ and $\beta = 2.471$ (Dyau and Kyriakides, 1993b). The main parameters of the individual tubes tested in water are listed in Table 1 and those tested in air in Table 2.

In both sets of experiments, the velocity was measured from pressure levels slightly higher than the propagation pressure to values close to the collapse pressure. The tubular test specimens originated from 20 different tubes each approximately 20 ft (6 m) long with the same nominal dimensions and properties. The actual diameter, wall thickness and yield stress varied to some degree from tube to tube and this is responsible for the scatter seen in the results (the normalization used reduces some of the scatter but not all of it). Overall, buckles travel faster when air is the pressurizing medium as opposed to water at the same pressure. For example, for pressure in the neighborhood of $4P_P$ the air velocity is of the order of 1000 ft/s (305 m/s), whereas in water it is of the order 800 ft/s (244 m/s). This shows that the added mass of the pressurizing fluid plays a role in the dynamics of buckles as suggested in Kyriakides and Babcock (1979) (see also Song and Tassoulas, 1993).

2.2.2. *Length of buckle profile*

Kyriakides (1980) used the signals from strain gages, mounted onto the tubes in a fashion similar to what was done here, to estimate the lengths of the buckle profiles as a function of the initiation pressure. For the

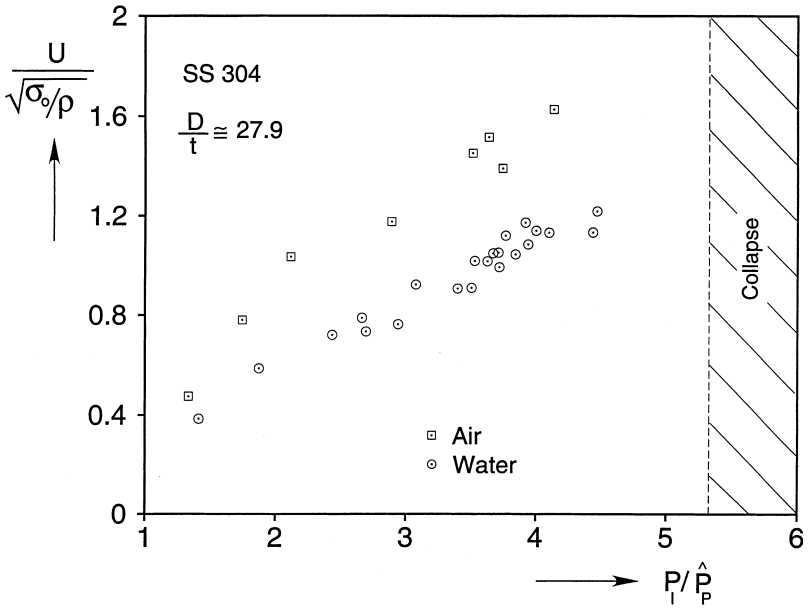

Fig. 4. Buckle velocity of propagation as a function pressure for water and air experiments.

aluminum tubes ($D/t = 35.7$) tested, he found that the profile of the buckle sharpened considerably as the initiation pressure was increased. The length of the profile (a) decreased from approximately $8D$ just above the propagation pressure to approximately $2D$ close to the collapse pressure. Further, the profile length, to first order, was inversely proportional to $\sqrt{P_I/P_P - 1}$.

We used the same method to estimate the lengths of the buckle profiles in our dynamic experiments. We have seen (Fig. 3(b)) that as the buckle passes by a particular strain gage, the axial strain recorded, undergoes a change in sign due to the switch in curvature associated with the buckle profile. We designate the time interval associated with the passage of the buckle by a strain gage as ΔT_p and use the measured buckle velocity (U) to estimate the profile length (a) from

$$a \approx U\Delta T_p. \tag{2}$$

Eq. (2) was used to estimate buckle profile lengths for most of the experiments conducted. The estimate was based on the signals from gages G2 and/or G3. Fig. 5 shows a plot of several of the profile length estimates normalized by the tube diameter versus the normalized pressure. The results from several air and water experiments are included. The profile length at quasi-static propagation was estimated to be approximately $6.5D$. Despite the relatively crude measurement technique used, the trend is quite clear. As the pressure increases, the buckle profile decreases quite considerably. Most of the sharpening of the profile occurs for pressures lower than $2P_P$, while subsequently the profile length stays within the range of $2.8D$ to $3.3D$. In general, the profile lengths are a bit shorter in the air experiments than those in water at the same pressure. This difference is attributed to the higher buckle velocity of the air experiments.

2.2.3. Flip–flop mode of buckle propagation

In the course of measuring the velocity of propagating buckles as a function of pressure, Kyriakides (1980) discovered the *flip–flop* mode of buckle propagation. He found that when a buckle was initiated in a long tube loaded to a pressure level of the order of 90% of the collapse pressure of the intact tube, or higher,

Table 1
Buckle velocities at various levels of pressure and tube parameters for water experiments

D, in. (mm)	t, in. (mm)	σ_0, ksi (MPa)	P_I, psi (bar)	$P_I/\hat{P}_P$	U, ft/s (m/s)
1.746 (44.35)	0.0617 (1.567)	46.0 (317)	1818 (125.3)	4.092	694 (212)
1.747 (44.37)	0.0629 (1.598)	45.1 (311)	1780 (122.7)	4.099	742 (226)
1.750 (44.45)	0.0642 (1.631)	39.4 (271)	1762 (121.5)	4.438	694 (211)
1.746 (44.35)	0.0618 (1.570)	46.0 (317)	1748 (120.5)	3.918	795 (242)
1.750 (44.45)	0.0637 (1.618)	39.0 (269)	1725 (117.5)	4.469	742 (226)
1.746 (44.35)	0.0628 (1.595)	44.5 (307)	1681 (115.9)	3.937	706 (215)
1.753 (44.53)	0.0653 (1.659)	43.2 (298)	1659 (114.3)	3.667	673 (205)
1.747 (44.37)	0.0622 (1.580)	46.0 (317)	1654 (114.0)	3.841	691 (211)
1.746 (44.35)	0.0619 (1.572)	44.5 (306)	1650 (113.7)	3.999	742 (226)
1.746 (44.35)	0.0628 (1.595)	44.5 (307)	1584 (109.2)	3.710	684 (208)
1.747 (44.37)	0.0621 (1.577)	46.0 (317)	1555 (107.2)	3.626	673 (205)
1.746 (44.35)	0.0619 (1.572)	44.5 (306)	1553 (107.0)	3.764	729 (222)
1.750 (44.45)	0.0639 (1.623)	39.4 (271)	1459 (100.6)	3.717	608 (185)
1.746 (44.35)	0.0620 (1.575)	46.0 (317)	1454 (100.2)	3.399	599 (183)
1.746 (44.35)	0.0618 (1.570)	44.5 (306)	1450 (99.9)	3.528	663 (202)
1.748 (44.40)	0.0622 (1.580)	46.9 (323)	1349 (93.0)	3.078	616 (188)
1.750 (44.45)	0.0636 (1.615)	39.0 (269)	1348 (92.9)	3.506	554 (169)
1.748 (44.40)	0.0622 (1.580)	46.9 (323)	1168 (80.5)	2.665	527 (161)
1.752 (44.50)	0.0641 (1.628)	39.0 (269)	1150 (79.3)	2.942	465 (142)
1.748 (44.40)	0.0623 (1.582)	46.9 (323)	1073 (73.9)	2.439	481 (147)
1.750 (44.45)	0.0640 (1.626)	39.7 (274)	1071 (73.8)	2.696	451 (137)
1.752 (44.50)	0.0670 (1.702)	39.9 (271)	825 (56.9)	1.873	358 (109)
1.752 (44.50)	0.0670 (1.702)	39.9 (272)	622 (42.9)	1.412	236 (72)

Table 2
Buckle velocities at various levels of pressure and tube parameters for air experiments

D, in. (mm)	t, in. (mm)	σ_0, ksi (MPa)	P_I, psi (bar)	$P_I/\hat{P}_P$	U, ft/s (m/s)
1.753 (44.53)	0.0658 (1.671)	43.2 (298)	1676 (115.6)	3.636	972 (296)
1.751 (44.48)	0.0645 (1.638)	37.5 (259)	1579 (108.9)	4.134	972 (296)
1.753 (44.53)	0.0651 (1.653)	43.2 (298)	1577 (108.8)	3.512	931 (284)
1.751 (44.48)	0.0638 (1.621)	40.0 (276)	1485 (102.4)	3.741	858 (262)
1.754 (44.55)	0.0649 (1.648)	43.2 (298)	1287 (88.8)	2.892	754 (230)
1.749 (44.43)	0.0660 (1.676)	44.4 (306)	1016 (70.1)	2.116	673 (205)
1.749 (44.43)	0.0661 (1.679)	44.4 (306)	841 (58.0)	1.745	507 (155)
1.749 (44.43)	0.0661 (1.679)	44.4 (306)	644 (44.4)	1.336	308 (93.9)
1.748 (44.40)	0.0653 (1.659)	45.5 (314)	2050 (141.4)	4.274	F–F

the following events took place. The buckle propagated a certain distance down the tube and then the direction of collapse rotated by 90°. The buckle propagated some distance in the new orientation and then switched orientation once more returning back to the original collapse mode. The process was repeated several times until the end of the tube was reached. Several such experiments were conducted on Al-6061-T6 tubes of D/t of 35.7 and 47.6 at pressures ranging from approximately $0.91P_{CO}$ to $0.99P_{CO}$ which confirmed the repeatability of the phenomenon.

The phenomenon was also encountered in several of the present experiments. For example, several flip–flops were obtained in an experiment on a SS-304 tube $48D$ long pressurized by air to 2050 psi (141.4 bar) in the test facility shown in Fig. 1. The buckle was initiated at one of the ends, propagated a distance of $10.6D$ from the point it was impacted and flipped. It flipped two more times further downstream at successive

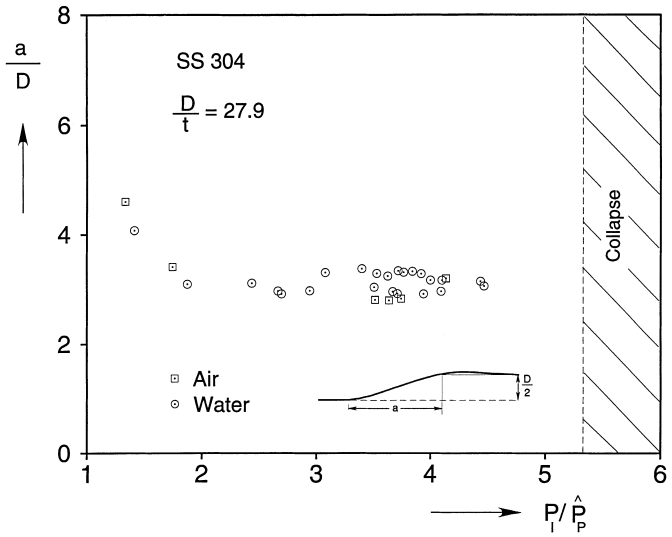

Fig. 5. Buckle profile length estimated from the strain gage signals vs. the initiation pressure.

distances of 10.3D and 11.1D. The photograph in Fig. 6(a) shows two of the nodes formed by the flipping of the collapse mode. An enlarged view of one of the nodes can be seen in Fig. 6(b). The geometric and material properties of this particular tube are listed in the last row of Table 2. Using these parameters and an initial ovality of 0.2%, its collapse pressure was estimated to be 2350 psi (162.1 bar). Thus, for this tube, the flip–flop mode occurs (for certain) for values of pressure higher than $0.87P_{CO}$ but possibly also at somewhat lower values.

Kyriakides (1980) used high speed photography to capture the flipping of the collapse mode. The experiments were conducted in a transparent acrylic pressure vessel with a pressure capacity of 240 psi (16.5 bar). The tubes used were Al-6061-T6 with a diameter of 1 in. (25.4 mm) and a D/t of 47.6. They had a collapse pressure of 205 psi (14.1 bar). A sequence of seven photographs from one of these experiments conducted at an air pressure of 192 psi (13.2 bar) is shown in Fig. 7 (corresponds to Fig. 4.5 of Kyriakides (1980) enhanced recently using the Adobe Photoshop software). The photographs were recorded at 4000 frames and thus they are separated by time intervals of 250 ns. The buckle is seen entering the viewing field traveling from left to right at a velocity of 790 ft/s (241 m/s). The tube is seen collapsing in the plane of the photographs. Ahead of the buckle front, there is a visible zone of reverse ovalization extending over a length of approximately 10D. In views ① to ④, the buckle propagates to the right with the zone of reverse ovality just ahead of it. Between views ⑤ and ⑥, the reverse ovality grows sufficiently to become critical for the existing ambient pressure. This region of the tube collapses and, in the process, initiates a propagating buckle at a new site. The new buckle is oriented at 90° to the original one. The original buckle and the new one run into each other forming the node seen in view ⑦. The node is similar to those from the tube tested in the present study shown in Fig. 6.

From the high speed photographic results and from measurements made on the tubes tested, Kyriakides (1980) concluded that the flipping of buckles is due to the following: Local flattening of a long cylindrical shell, say, by a pair of diametrically opposite point or line loads, results in a secondary ovalization, some distance (a few radii) away from the local flattening. The major axis of this ovalization is oriented at 90° to the major axis of the applied flattening and extends over a length of a few radii. The reverse ovality also occurs in thin elastic shells (Yuan, 1946; Yuan and Ting, 1957) but is amplified significantly as the cylinder

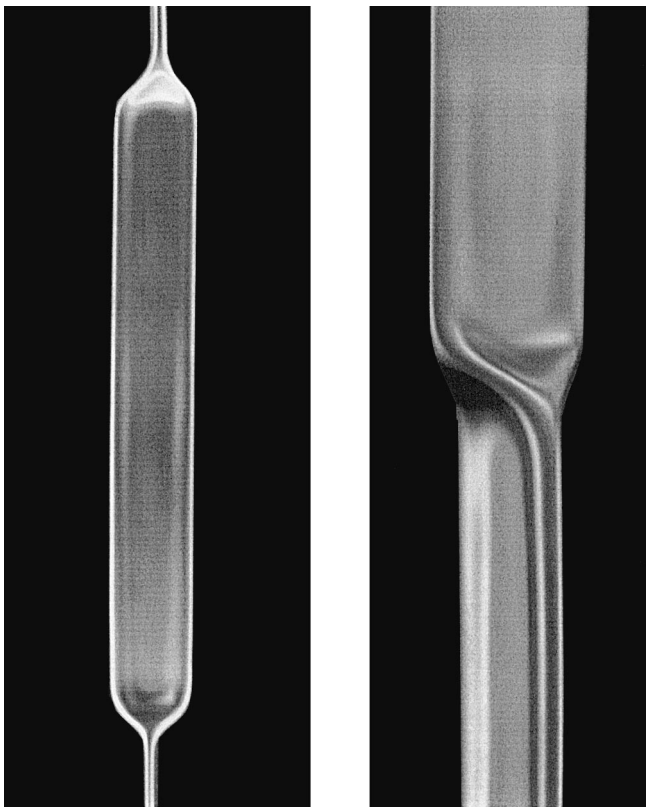

Fig. 6. Flip–flop mode of buckle propagation as recorded in an experiment on a SS-304 tube with $D/t = 26.8$: (a) Two changes in buckle propagation mode. (b) Detail of a flip–flop node.

is crushed plastically (Reid et al., 1976; Kyriakides, 1980). Thus, ahead of any propagating buckle there always exists a zone of reverse ovality (see Dyau and Kyriakides, 1993a,b; Netto and Kyriakides, 2000b). The extent of the reverse ovality depends on the profile length.

Once initiated, buckles accelerate to a steady-state velocity which is determined by the pressure, the pressurizing fluid and the tube geometric and material parameters. As the buckle accelerates, its front sharpens as reported above. This sharpening of the front increases the reverse ovality induced to the section of tube just downstream of the buckle. The higher the pressure, the larger the amplitude of the reverse ovality. At some pressure level, the reverse ovality is sufficiently large to cause collapse in the manner shown in Fig. 7. The new local collapse accelerates to a speed at which the buckle front has shortened sufficiently to induce a new zone of critical reverse ovality ahead of it and the events are repeated. These conclusions will be scrutinized in the next section in the light of numerical results.

2.2.4. Strain rate effects

In the range of buckle velocities reported in Tables 1 and 2, points on the collapsing cross-section of the tubes can reach very high strain rates ($\dot{\varepsilon}$). From the strain gage signals, $\dot{\varepsilon}$ is estimated to be in the range of

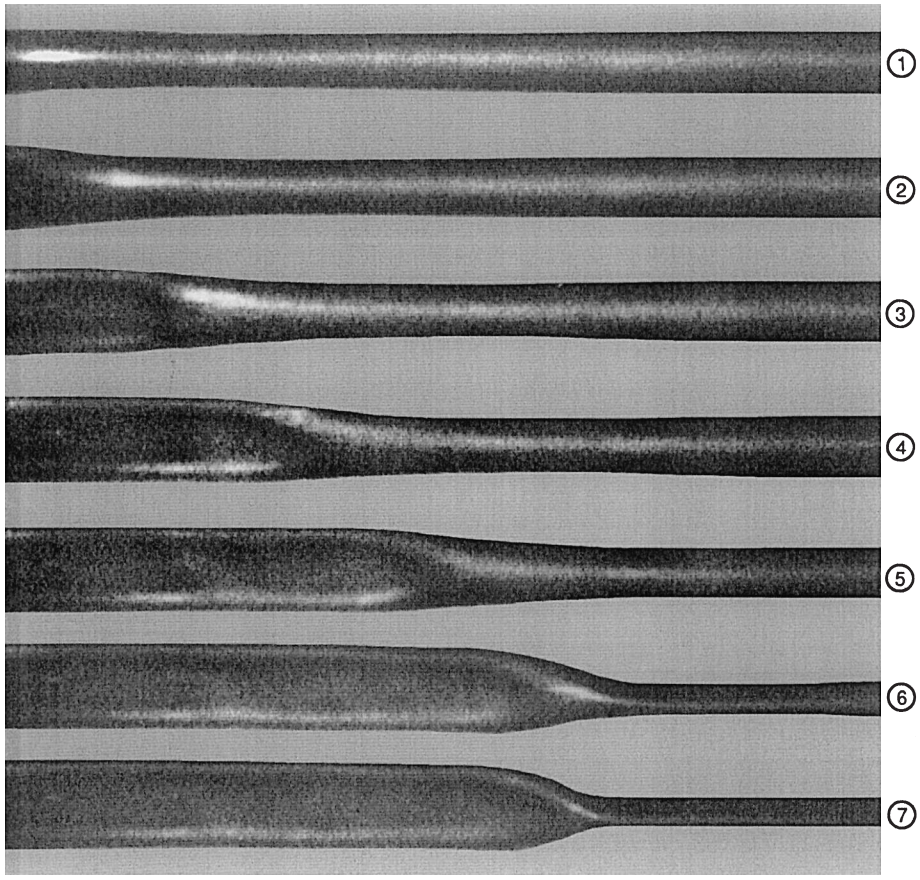

Fig. 7. Sequence of high speed photographs showing the flip–flop mode of buckle propagation (Al-6061-T6, $D/t = 47.6$, $P_1/\hat{P}_{CO} = 0.934$, 4000 frames; from Kyriakides (1980)).

200–800 s^{-1} for the water experiments and 800–1200 s^{-1} for the air experiments. At strain rates of these levels, the mechanical behavior of steels changes significantly and this change must be taken into account in the analysis of the problem. The rate dependence of our stainless steel material was established in a series of uniaxial tension tests performed at prescribed values of constant strain rate. The flow stress at rates of the order of 10^2 and higher is usually established from Hopkinson bar experiments. Results from such experiments on SS-304L spanning rates of $\dot{\varepsilon} \in (10^{-4}, 10^4)$ were reported in Stout and Follansbee (1986). Their results are summarized in Fig. 8 in a plot of the true stress (σ_t) at a logarithmic strain (e) of 0.1 versus the true strain rate. At a strain rate of approximately 10^2, the flow stress undergoes a dramatic increase in its rate dependence. Included in the same plot are results from the more limited study we performed on the tube material. Although the actual values of the flow stresses of the two stainless steels at any given strain rate differ, their trend with the rate is similar. In the calculations that follow, we will assume that this similarity in the rate dependence of the two materials continues at higher rates. With this assumption, the material is modeled through the classical overstress powerlaw viscoplastic model in which the plastic strain rate is assumed to obey the following rule:

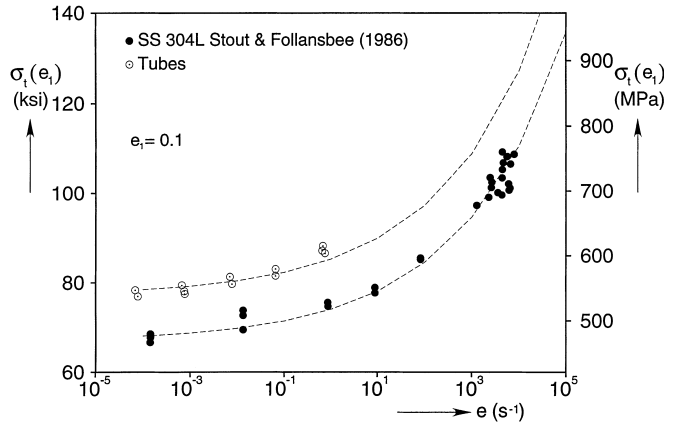

Fig. 8. True flow stress as a function of strain rate for tube material compared with results of Stout and Follansbee for a similar alloy.

$$\dot{\varepsilon}^{\mathrm{p}} = D\left(\frac{\sigma}{\Sigma(\varepsilon^{\mathrm{p}})}\right)^{m'}. \tag{3}$$

Here $\Sigma(\varepsilon^{\mathrm{p}})$ is the flow stress measured at a low base strain rate ($\dot{\varepsilon} = 10^{-4}$). $D = 80 \times 10^3$ and $m' = 5$ were found to reproduce the sensitivity to rate measured by Stout and Follansbee (dashed lines in Fig. 8).

3. Analysis

3.1. Finite element model

The dynamic propagation of buckles and their engagement with integral buckles arrestors was recently investigated by Netto and Kyriakides (2000b) using a finite element model developed within the nonlinear code ABAQUS. The calculations performed were limited to the case of buckle propagation in vacuum. We expect this to be representative of experiments conducted in air where the role of the inertia of the pressurizing fluid is small. Here, we use the same model and numerical procedures to study the initiation and steady-state dynamic propagation of buckles and the problem of flipping of buckles.

The model consists of a section of tube length L. The deformation of the tube cross-section is assumed to have two planes of symmetry (planes 1, 2 and 1–3 in Fig. 9). In addition, planes 2, 3 passing through the location at which the propagating buckle is initiated, is also assumed to be a plane of symmetry. The tube is discretized with three-dimensional, 27-node, quadratic brick elements (C3D27R) with reduced integration. In the axial direction, the model is discretized with elements approximately $0.71D$ long. In the circumferential direction, the 90° sector is discretized with 10 elements with the following angular spans (starting from the x_2-axis): 10°–10°–15°–15°–10°–10°–7.5°–7.5°–2.5°–2.5°. Two elements are used through the thickness.

Contact is simulated by using the surface-based contact modeling. This model prevents the nodes that define the inner surface of the tube from penetrating the planes of symmetry which are made to be rigid (R3D4).

The boundary nodes at $x_1 = L$ are constrained in the radial and circumferential directions and are free to move in the x_1-direction. Symmetry conditions are imposed at the nodes at $x_1 = 0$, $x_2 = 0$ and $x_3 = 0$. Unless otherwise stated, the tubes will be assigned the same geometric properties as those used in the study

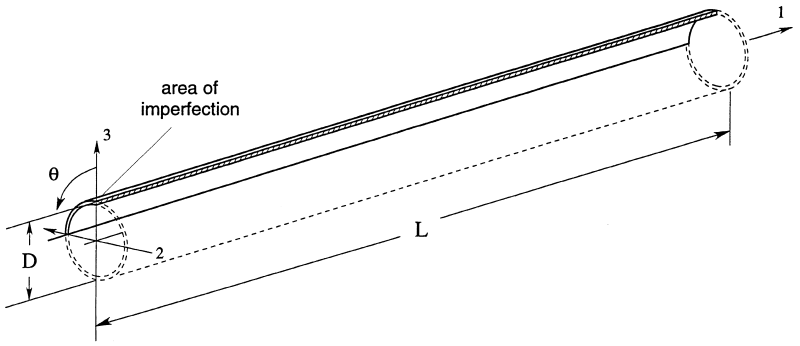

Fig. 9. Geometry of the tube analyzed and co-ordinate system.

Table 3
Geometric and material parameters of tubes used in this study

	D, in. (mm)	t, in. (mm)	E, msi (GPa)	σ_0, ksi (MPa)	σ_y, ksi (MPa)	n	ρ lb in.$^{-3}$ (kg m^{-3})
Average values	1.748 (44.40)	0.0627 (1.59)	29.2 (205)	43.84 (301.7)	39.6 (272)	12	0.280 (7750)
F–F exp.	1.748 (44.40)	0.0653 (1.659)	28.7 (200)	45.5 (314)	41.0 (283)	10.5	0.280 (7750)

of dynamic arrest of buckles given in the first row of Table 3 (taken from Netto and Kyriakides, 2000a). These dimensions represent the mean values of the whole set of tubes used in the broader study of dynamics of buckles performed by the authors.

A buckle is initiated from a local imperfection in the form of ovality in the neighborhood of the symmetry plane ($x_1 = 0$) defined by

$$\frac{w_0(\theta)}{R} = -\Delta_0 \exp\left[-\beta\left(\frac{x}{D}\right)^2\right]\cos 2\theta, \tag{4}$$

where w_0 is the radial displacement, θ is the polar angular coordinate and x is the axial coordinate. The amplitude Δ_0 is chosen to fit the needs of the case analyzed and the constant β decides the extent of the imperfection (usually limited to one tube diameter).

3.2. Constitutive model

The material is modeled as an elastic/powerlaw overstress viscoplastic solid. The strain rates are assumed to consist of an elastic part and an inelastic part

$$\dot{\underline{\varepsilon}} = \dot{\underline{\varepsilon}}^{\mathrm{e}} + \dot{\underline{\varepsilon}}^{\mathrm{p}}. \tag{5}$$

Elastic deformations are linear and isotropic and are related to stresses by

$$\dot{\underline{\varepsilon}}^{\mathrm{e}} = \frac{1+\nu}{E}\dot{\underline{\sigma}} - \frac{\nu}{E}(\mathrm{tr}\,\dot{\underline{\sigma}})\underline{I} \quad \text{or} \quad \dot{\underline{\sigma}} = \underline{C}(E,\nu)\dot{\underline{\varepsilon}}^{\mathrm{e}}, \tag{6}$$

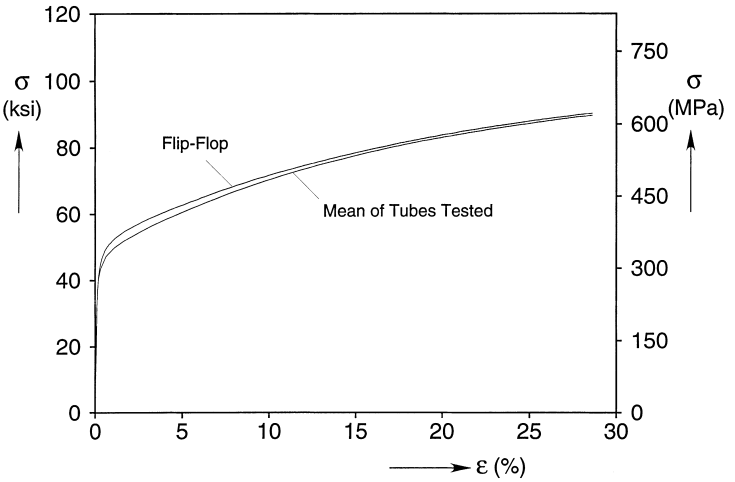

Fig. 10. Mean stress–strain response of the tubes used in the experiments and the one for the tube used in the flip–flop experiment reported.

where E is Young's modulus and v, Poisson's ratio of the material, both assumed to be independent of rate. The inelastic part of the deformation ($\dot{\underline{\varepsilon}}^{\mathrm{p}}$) is assumed to exhibit an overstress powerlaw rate dependence, which for a uniaxial state of stress is given by Eq. (3) (Malvern, 1951; Ripperger, 1965). The model is calibrated to the base stress–strain response shown in Fig. 10 fitted with approximately 40 linear segments of unequal strain span. The constants D and m' were selected as described in Section 2.2.4.

The model was generalized to the multiaxial setting through the classical associative plasticity framework (e.g. see Peirce et al., 1984). The plastic strain is given by

$$\dot{\underline{\varepsilon}}^{\mathrm{p}} = \Lambda \frac{\partial f}{\partial \underline{\sigma}} \tag{7a}$$

with the following choice for f:

$$f = \sigma_{\mathrm{e}} = \sqrt{\tfrac{3}{2}\underline{s}\cdot\underline{s}}, \quad \underline{s} = \underline{\sigma} - \tfrac{1}{3}(\mathrm{tr}\,\underline{\sigma})\underline{I}. \tag{7b}$$

A work compatible measure of equivalent strain rate is

$$\dot{\varepsilon}^{\mathrm{p}}_{\mathrm{e}} = \sqrt{\tfrac{2}{3}\dot{\underline{\varepsilon}}^{\mathrm{p}}\cdot\dot{\underline{\varepsilon}}^{\mathrm{p}}}. \tag{7c}$$

Thus, Eqs. (3), (7b) and (7c) $\rightarrow$ (7a) yield

$$\dot{\underline{\varepsilon}}^{\mathrm{p}} = \dot{\varepsilon}^{\mathrm{p}}_{\mathrm{e}}\left(\frac{3}{2}\frac{\underline{s}}{\sigma_{\mathrm{e}}}\right) = D\left(\frac{\sigma_{\mathrm{e}}}{\Sigma(\varepsilon^{\mathrm{p}}_{\mathrm{e}})} - 1\right)^{m'}\left(\frac{3}{2}\frac{\underline{s}}{\sigma_{\mathrm{e}}}\right), \tag{8a}$$

where

$$\varepsilon^{\mathrm{p}}_{\mathrm{e}} = \int_0^t \dot{\varepsilon}^{\mathrm{p}}_{\mathrm{e}}\,\mathrm{d}t. \tag{8b}$$

By combining Eqs. (8a), (8b) and (6) through Eq. (5) and inverting we arrive at

$$\dot{\underline{\sigma}} = \underline{C}\dot{\varepsilon} - \left(\frac{3\dot{\varepsilon}_e^p}{2\sigma_e}\right)\underline{Cs}. \tag{9}$$

4. Numerical results

4.1. Quasi-static buckle propagation

We first briefly review the quasi-static version of the problem, the solution of which will help illustrate the changes induced to the front of the propagating buckles by dynamics. Dyau and Kyriakides (1993a,b) traced the unstable path followed by tubes collapsed by external pressure by prescribing the change in the internal volume of the tube (usually a monotonically increasing variable). In the present calculations, the hydrostatic fluid elements of ABAQUS is employed instead (a combination of F3D3 and F3D4). These elements allow prescription of the change in volume inside a control region defined around the structure which is an equivalent method of volume control. In both the schemes, the pressure becomes an additional unknown while the volume change is enforced as a constraint via the Lagrange multipliers method. For quasi-static calculations, the material is modeled as a J_2 flow theory solid with isotropic hardening calibrated to the base stress–strain response given in Fig. 10 (mean curve).

The pressure change in volume $(\delta v/v_0)$ response calculated for the present tube is shown in Fig. 11 (v_0 is the initial volume of the tube and $\hat{P}_{CO}$ is the calculated collapse pressure of the tube, 2184 psi (150.6 bar)). Fig. 12 shows a set of deformed configurations of the tube generator $(x, 0)$ which correspond to the numbered points marked on the $\overline{P}$–$\delta\overline{v}$ response. Due to the localized imperfection the pressure reaches a maximum at 1945 psi (134.1 bar) and subsequently the tube collapses locally as described in Dyau and Kyriakides (1993a,b). The local collapse is arrested when the walls of the tube come into contact (configuration ④). This corresponds to the local minimum in the $\overline{P}$–$\delta\overline{v}$ response. Subsequently, the collapse starts to propagate down the length of the tube and quickly reaches steady-state propagation conditions (configurations ⑤ to ⑨) tracing the pressure plateau seen in Fig. 11. This is the propagation pressure $(\hat{P}_P)$ of the tube which is 425 psi (29.3 bar). This value is in very good agreement with the measured results (Netto and Kyriakides, 2000a).

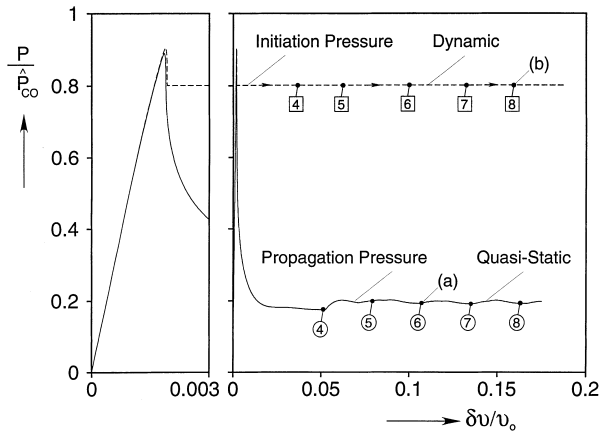

Fig. 11. Simulated pressure-change in volume responses for quasi-static and dynamic propagation of buckles.

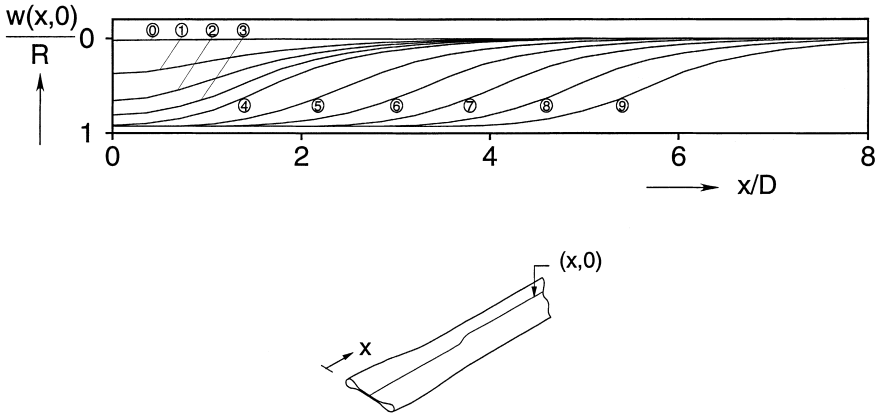

Fig. 12. Sequence of deformed contours of generator $(x, 0)$ for quasi-static buckle propagation corresponding to the points marked on response in Fig. 11.

A full view of buckled configuration ⑥ rendered through the SunVision image processing system and edited via the Adobe Photoshop software is shown in Fig. 13(a). The crown points of the collapsed cross-section behind the front are in contact essentially along an axial line. The deformed generator $(x, 0)$

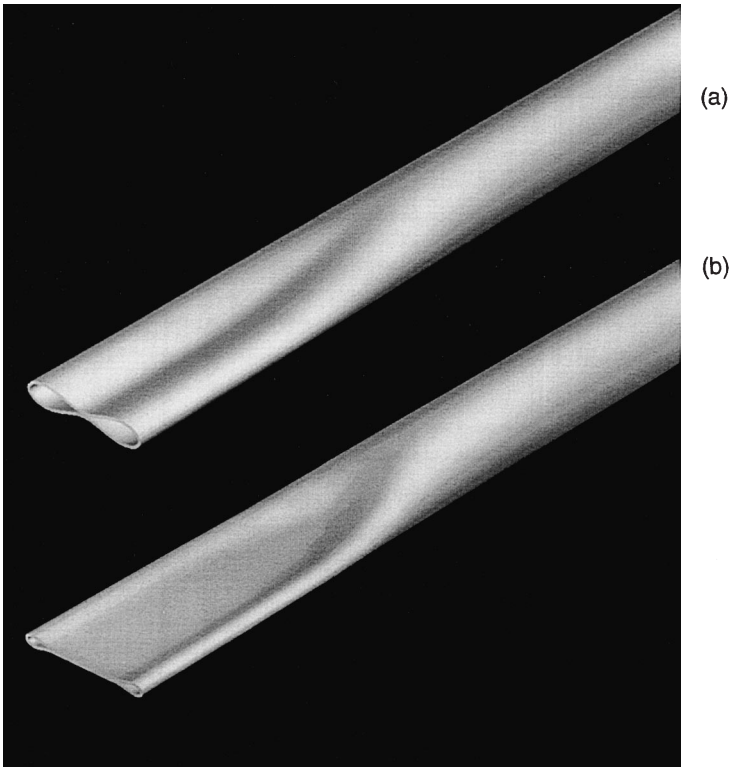

Fig. 13. Tube calculated deformed configurations during steady-state: (a) Quasi-static propagation and (b) dynamic propagation ($U = 1100$ ft/s, 335 m/s).

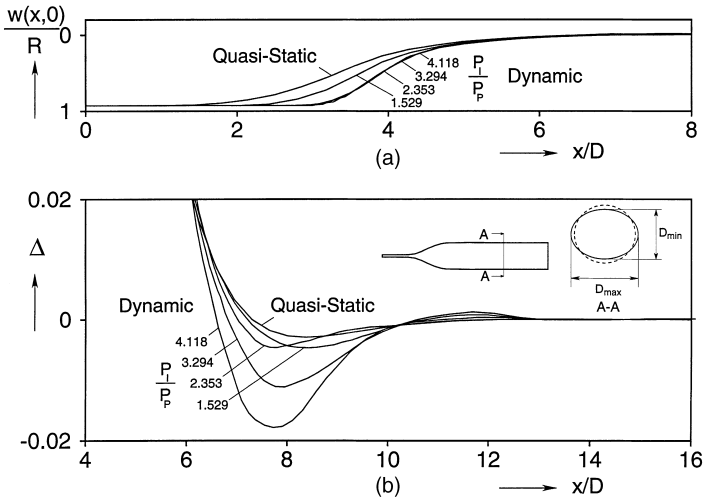

Fig. 14. (a) Comparison of deformed contours of specimen generator $(x, 0)$ from quasi-static and dynamic solutions at four levels of pressure. (b) Expanded contours of same generator showing tube reverse ovalization ahead of the buckle fronts.

corresponding to this configuration is plotted in Fig. 14(a). The length of the profile, defined as the distance between the first points on either side of the generator to reach zero slope, is approximately $6.4D$. Adjacent to the buckle profile is a zone of reverse ovality not discernible in the scale of Figs. 13 and 14(a). The ovality (Δ) of this section of tube was calculated using the definition

$$\Delta = \frac{D_{\max} - D_{\min}}{D_{\max} + D_{\min}}. \tag{10}$$

The calculated values are plotted against the axial coordinate in Fig. 14(b). Reverse ovalization is seen to extend over a length of approximately 4.5 tube diameters. Its maximum value is approximately 0.32%.

4.2. Dynamic buckle propagation

4.2.1. A characteristic example

A brief description of the formulation and numerical procedures used in ABAQUS for dynamic calculations is given in Appendix A (based on implicit integration). As in the experiments, there are several possible ways of initiating the collapse. For numerical expediency, dynamic buckles are initiated as follows: The tube is loaded by external pressure using Riks' path following scheme to follow the loading history past the pressure maximum. The subsequent unstable regime is followed until the pressure drops to the level chosen for the dynamic test (dashed line in Fig. 11). The pressure is fixed at the desired level and a switch is made to the dynamic version of the model. The last equilibrium solution of the quasi-static analysis is given a small perturbation (usually at $x = 0$, where the imperfection has the largest amplitude) and the dynamic solution is followed by appropriate time integration. For the tube discussed above, the maximum pressure is 1945 psi (134.1 bar). The pressure is allowed to drop to 1750 psi (120.7 bar), its value is fixed and the dynamic analysis is commenced.

Fig. 15 shows the initial and a sequence of deformed configurations of the tube generator $(x, 0)$ from this dynamic calculation. Several of the configurations are identified by numbered bullets marked on the $\overline{P}$–$\delta\overline{v}$

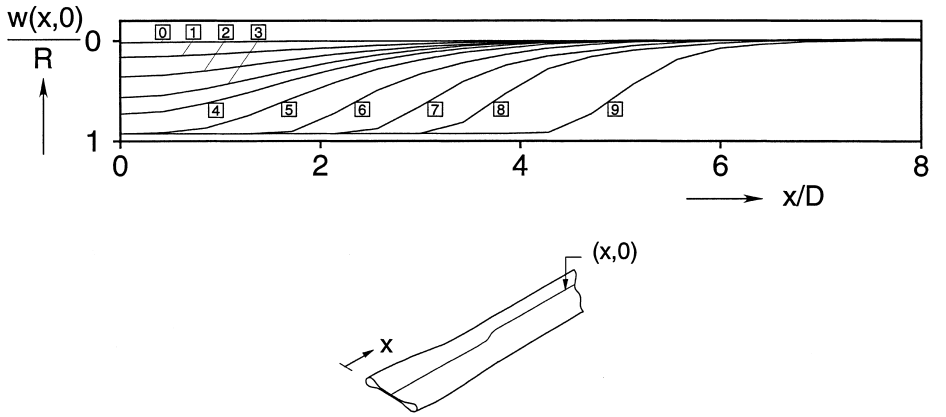

Fig. 15. A sequence of deformed contours of generator $(x, 0)$ showing the initiation and subsequently steady-state dynamic propagation of a buckle at $P_I = 1750$ psi (120.7 bar).

response in Fig. 11. The extent of local collapse is initially similar to that from the quasi-static solution. On the way down the collapsing walls (configurations [1] to [4]) accelerate. Configuration [5], which approximately corresponds to the first contact of the crown points of the collapsed section, reaches 0.518 ms into the dynamic simulation. Subsequently, the buckle propagates down the length of the tube. During this process, the profile of the buckle sharpens and by configuration [7] ($T = 0.658$ ms), a steady state is achieved where the buckle is propagating at a constant velocity of approximately 1100 ft/s (335 m/s). A linear fit of the buckle velocities measured in the experiments in this pressure regime yielded a value of 1035 ft/s (315 m/s) for this pressure.

A rendering of the calculated profile of the buckle in the steady-state conditions is shown in Fig. 13(b), while the corresponding deformed contour of the generator $(x, 0)$ is included in Fig. 14(a) ($P_I/\hat{P}_P = 4.118$). The differences between the profile at the propagation pressure and the present one are significant. In the dynamic case, the tube behind the buckle is essentially flattened by the much higher ambient pressure and by the inertial forces. This results in the much sharper buckle profile seen clearly in Figs. 13 and 14(a). The length of the profile is now $3.3D$, i.e., down to almost half the length of the profile at $\hat{P}_P$. This value is in reasonable agreement with corresponding values estimated from the strain gage signals shown in Fig. 5.

This sharpness of the collapse profile in turn causes a significant increase in the amplitude and to some degree the extent the reverse ovality induced to the tube downstream of the buckle profile. This is illustrated in the expanded contour detail included in Fig. 14(b) (again look at $P_I/\hat{P}_P = 4.118$). Reverse ovality now extends over a section of four tube diameters long while the amplitude of the maximum ovality has increased to 1.8% or approximately six times the amplitude at the propagation pressure.

In order to delineate the effect of material rate dependence on the dynamics of buckles, we conducted a similar calculation in which the material was modeled as a rate independent J_2 flow theory solid which hardens isotropically. The stress–strain response used to calibrate the model is the one (mean) shown in Fig. 10. The processes of dynamic collapse, localization and steady-state propagation are very similar. The buckle velocity at steady-state was essentially the same (~1100 ft/s to 335 m/s). The buckle profile for this calculation is compared to that from the rate dependent case in Fig. 16. The profile is very similar but the region of reverse ovality (Fig. 16(b)) is somewhat larger in extent (~$4.3D$) and in amplitude ($\Delta = 2.3\%$) probably due to the lower yield stress of this material model. Thus, the rate dependence of SS-304 plays some role in the results but not as large as might be expected from the fact that points on the collapsing

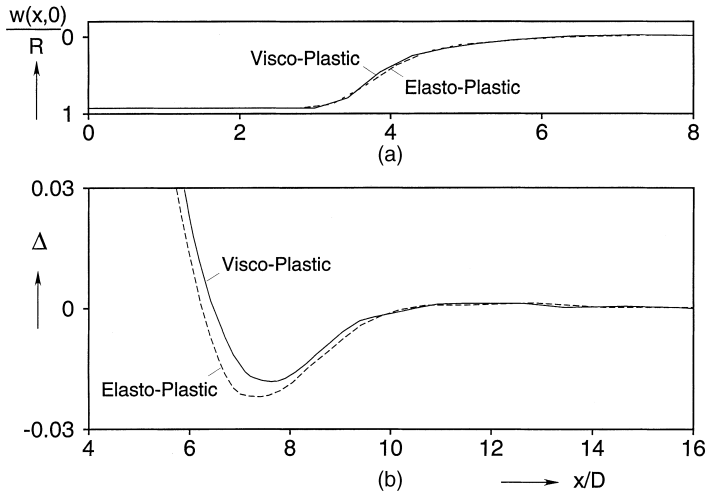

Fig. 16. Comparison between contours of generator $(x,0)$ from dynamic calculations using the J_2 flow theory and the visco-plastic overstress model.

cross-section, strain rates of the order of 10^3 s^{-1}. The main mechanism of collapse is bending and thus only small parts of the collapsing front experience these high strain rates (see Netto, 1998, Chapter 6).

4.2.2. Buckle velocity as a function of pressure

Dynamic calculations of the type described above were conducted for 12 cases with initiation pressures in the range $1.117 \leqslant P_I/\hat{P}_P \leqslant 4.118$ using the tube geometric and material parameters listed in Table 3 and Fig. 10. The calculated steady-state buckle velocities $(\hat{U})$ are plotted against the initiation pressure in Fig. 17 along with the experimental values (for the predictions, the normalizing variables are: $\hat{P}_P = 425$ psi to

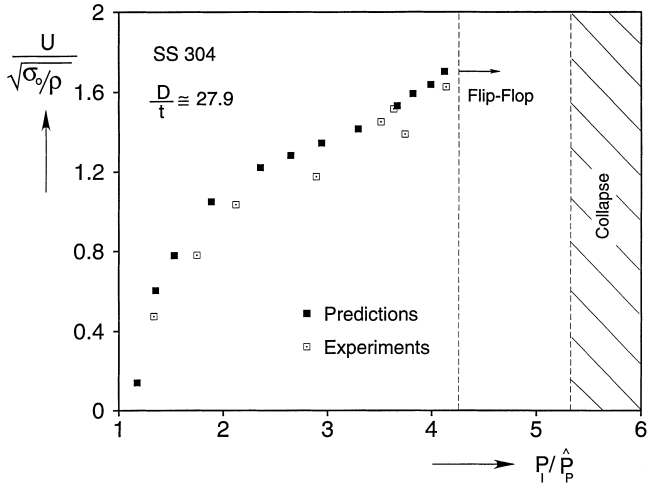

Fig. 17. Comparison of buckle velocities measured in experiments in air and predicted values for buckles propagating in vacuum.

29.3 bar and $\sqrt{\sigma_0/\rho} = 645$ ft/s to 196.6 m/s). The predicted velocities are seen to follow well the trend of the experimental values and to exhibit less scatter due to the constant tube variables used in the calculations. In this scheme, one-to-one comparison of measured and predicted velocities is not possible. However, clearly the predictions are generally somewhat higher than the measured values. In the experiments, air was present both inside the collapsing tubes as well as outside them. In the model the tubes collapsed in vacuum. Although the effect of the air is not considered to be very significant, it obviously had some effect which causes the measured velocities to be somewhat lower than the predictions.

4.2.3. Study of the buckle profile

The numerical simulations provided a more quantitative picture of how dynamics alters the profile of a propagating buckle. At each pressure level considered, the length of the profile of the buckle at steady state propagation (a) was estimated using the same definition of buckle profile as that used in the experiments. The values measured are plotted against the initiation pressure in Fig. 18. Included is the profile length for quasi-static propagation of the buckle ($a = 6.4D$). The buckle profile is seen to experience significant sharpening between $\hat{P}_P < P_I < 2.5\hat{P}_P$ when its length is reduced by nearly 40%. Interestingly, this pressure range corresponds to the values up to the formation of the first knee in the velocity–pressure plot in Fig. 17. The additional sharpening that takes place at higher pressures is rather modest. Despite the rather crude way the buckle profile was estimated in the experiments, the trend of the predictions is very similar to that in the corresponding experimental plot in Fig. 5 which is reassuring.

Contours of the generator $(x, 0)$ representing the dynamic buckle profiles at four pressures are compared to the quasi-static one in Fig. 14(a). The same tendency is seen here. The profile sharpens at lower pressures but remains relatively unchanged at higher pressures. As stated in the experimental section, sharpening of the profile beyond a certain point must involve significant membrane stretching which requires significantly more energy than the predominantly bending mechanism through which the buckle sharpens at lower pressures.

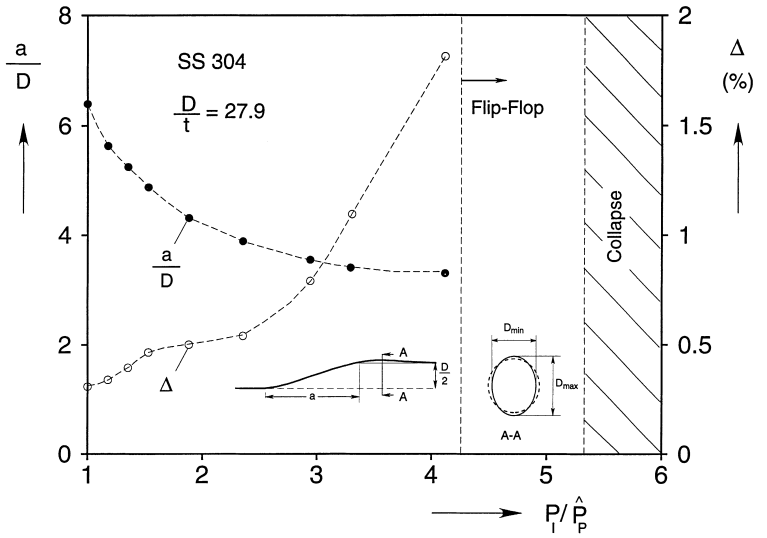

Fig. 18. Calculated values of buckle profile length and amplitude of corresponding induced reverse ovality as a function of pressure.

As discussed earlier, the sharpening of the profile of the buckle with pressure, coupled with the fact that the pressure is higher, result in an increase in the amplitude and, to some degree, the extent of the zone of reverse ovality that precedes the buckle profile. The amplitude of the reverse ovality of buckles propagating at steady-state was estimated from the numerical results using the definition in Eq. (10). The variable Δ is plotted against the initiation pressure in Fig. 18 (see also inset). At lower pressures the rate of growth of Δ with pressure is relatively modest. Around a pressure level of approximately $3\hat{P}_P$ its rate of growth with pressure experiences a very significant increase so that at a pressure of $4.118\hat{P}_P$ it reaches a value of 1.8%. The extent of reverse ovality can be seen in Fig. 14(b) where four dynamic profiles are compared to the quasi-static one.

4.2.4. Simulation of the flip–flop mode of buckle propagation

The highest value of pressure at which a dynamic buckle propagation calculation was performed is $4.118\hat{P}_P$ which corresponds to $0.80\hat{P}_{CO}$. The essentially powerlaw growth of reverse ovality with pressure seen in Fig. 18 indicates that, at some pressure level higher than this value, the reverse ovality may grow to a high enough value for the affected section of the tube to collapse. If this takes place, then a second buckle initiation site is created where the tube is collapsing at 90° to the original direction of collapse. We investigated this prospect as follows. A model was developed along the lines described in Section 4.2.1 but with a length of $24D$. In this case, the model was assigned the dimensions and mechanical properties of the tube used in the specific flip–flop experiment described in Section 2.2.3 (see Table 3 and Fig. 10). Using these characteristics and an initial ovality of 0.2%, the collapse pressure of this tube is estimated to be 2350 psi (162.1 bar) and its propagation pressure 480 psi (33.1 bar).

The buckle was initiated at the same pressure of 2050 psi (141.4 bar) at which it was initiated in the experiment ($P_I/\hat{P}_{CO} = 0.872$). Fig. 19 shows a sequence of deformed tube configurations obtained from the solution. The buckle is initiated in the manner described above in the neighborhood of the plane of symmetry $x = 0$. The process of localization of the buckle, the arrest of local collapse by contact, and the subsequent propagation of the buckle down the tube are the same as described in Section 4.2.1 (configurations ① to ③). As the buckle accelerates towards steady-state, the reverse ovality ahead of it grows. This is clearly seen in the sequence of truncated deformed contours of the tube generator $(x, 0)$ shown in Fig. 20(a). By configuration ④, the buckle has propagated a distance of approximately $8.5D$. The reverse ovality ahead of the buckle front reaches a critical amplitude triggering a new collapse event downstream of the propagating buckle. The onset of this unstable growth of reverse ovality can be seen in Fig. 20(a) and in more detail in the expanded view in Fig. 20(b). In configuration ⑤ in Fig. 19, the new buckle has already formed. The new mode of collapse is at 90° to the original one.

The newly initiated buckle goes through the same process of localization and propagation down the tube as the original one. The original buckle and the new one meet and engage each other forming the stationary node seen in configurations ⑥ to ⑧. The center of the node is at $x = 8.6D$. In the experiment, the buckle was initiated close to one of the ends of the tube which was sealed by inserting and bonding a solid plug into the end. This is close to a fixed boundary condition which differs from the symmetry condition used at $x = 0$ in the model. Because of this difference, the distance from the initiation site to the first node is shorter in the model than it was in the experiment.

The second buckle propagates down the tube and flips once more forming a second node at a distance $9.8D$ downstream of the first one (not shown in Fig. 19). This compares well with the distance of $10.3D$ between the first two buckle nodes of the experiment.

Two views of the node formed by the flipping event are shown in Fig. 21. Its major characteristics are similar to the experimental node shown in Fig. 6. Its ridges are somewhat less severely deformed than in the experiment. This could be corrected by further refining the axial distribution of the FE mesh of this region and repeating the calculation. This was deemed unnecessary and was not carried out due to the very large computation time required by such calculations.

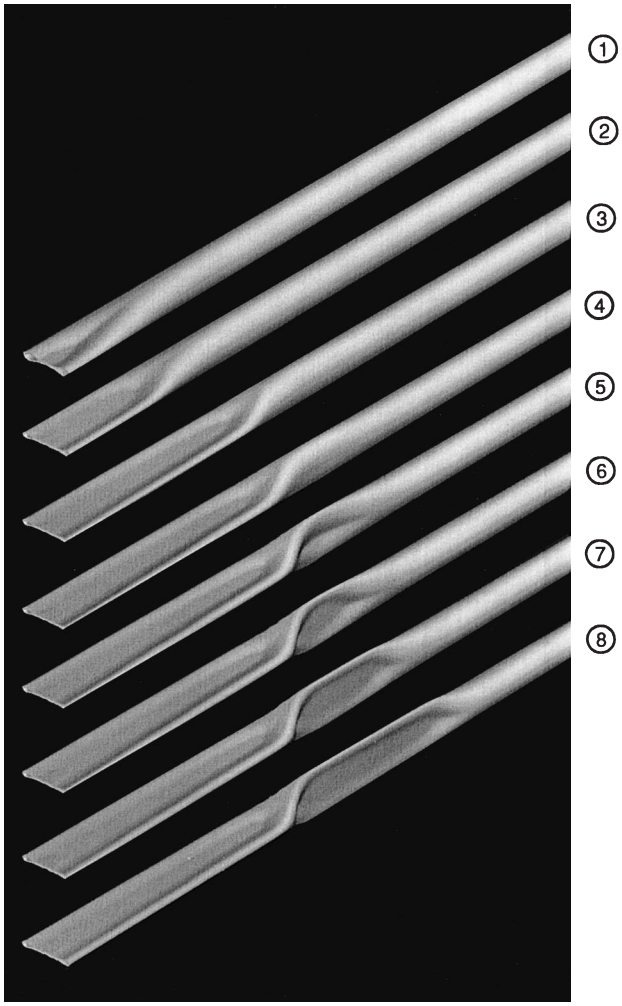

Fig. 19. Sequence of calculated deformed contours of tube collapsing dynamically showing the development of a flip–flop ($P = 2050$ psi, 141.4 bar).

5. Conclusions

The problem of dynamic propagation of buckles in long pipes under constant external pressure was investigated in part by Kyriakides, 20 years ago using relatively thin, model aluminum tubes. The present study includes new results from stainless steel tubes with $D/t = 27.9$. Each test specimen was placed in a constant pressure environment using either air or water as the pressurizing medium. The buckle was initiated at one of the ends of the specimen by impact; it was allowed to accelerate to steady-state and its velocity was recorded. The initiation pressures covered the range of $P_P < P_I < P_{CO}$. The following major findings are reported from the experiments:

(a) For a given pressure, the buckle was found to travel faster in air than in water, confirming that the inertia of the pressurizing fluid plays a role in the problem. In air, velocities as high as 1200 ft/s (365 m/s) were recorded, whereas in water, the highest values were approximately 800 ft/s (244 m/s).

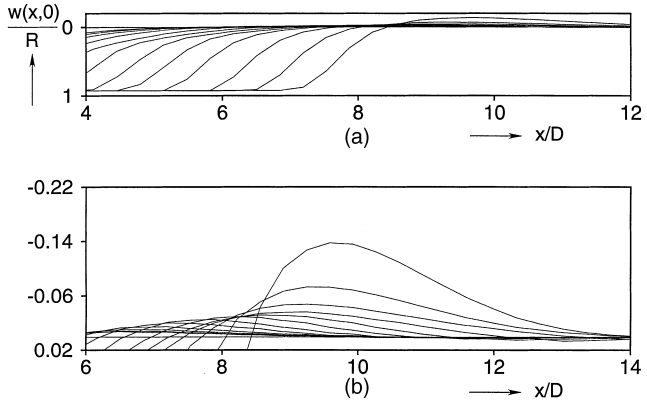

Fig. 20. (a) Sequence of deformed contours of part of the tube generator $(x, 0)$ showing the propagating buckle and onset of the flipping of the collapse mode. (b) Expanded view of generator showing the localization of the reverse ovality ahead of the buckle.

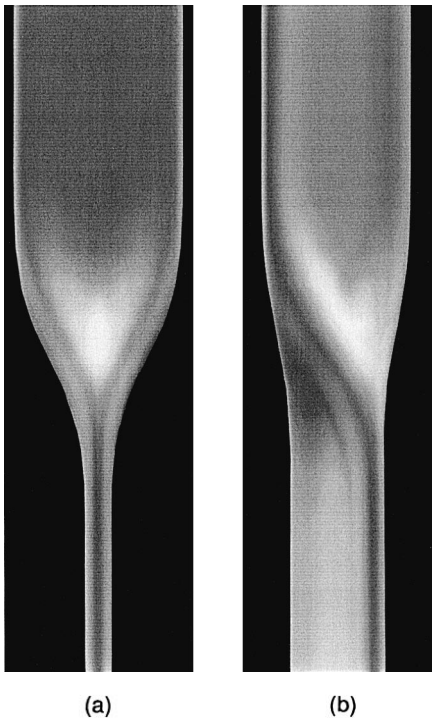

Fig. 21. Two views of the node of the flip–flop generated in the simulation shown in Fig. 19.

(b) The buckle front was found to sharpen significantly with pressure. When the initiation pressure reached a value of approximately $2.5P_{\mathrm{P}}$, the profile length was found to get reduced nearly by one half of its value at quasi-static propagation.
(c) For the tube tested, the flip–flop mode of buckle propagation was found to occur for pressures higher than $0.87\hat{P}_{\mathrm{CO}}$.

A model capable of simulating the dynamic initiation and propagation of such buckles has been developed within the FE code ABAQUS. The fluid-structure interaction problem has been bypassed at this stage by assuming buckling and collapse to take place in vacuum. The model accounts for the inertia of the pipe and the nonlinearity introduced by contact between the collapsing walls of the pipe. The material is modeled as a finitely deforming, elastic/powerlaw overstress viscoplastic solid. The model was used to calculate the velocity of propagation of the buckle as a function of the ambient pressure. The following conclusions can be drawn from the numerical results:

1. The calculated buckle velocities are compared with the values measured in the physical experiments in air. The predictions are somewhat higher than the measured velocities but follow the trend of the experimental results well.

2. The numerical simulations confirmed the sharpening of the buckle front with pressure. Most of the sharpening was found to occur between $P_P < P_I < 2.5P_P$. As was the case in the experiments, at higher pressures the additional decrease in the length of the buckle profile was very modest.

3. Just ahead of the propagating buckle front, the tube experiences some reverse ovality (Kyriakides, 1980). The amplitude of this reverse ovality was found to increase with pressure. This is caused by the sharpening of the buckle profile and by the pressure loading. Eventually, a pressure level is reached at which the reverse ovality is high enough for it to cause local collapse. This is responsible for the flip–flop mode of buckle propagation.

4. The model was shown to be capable of simulating the flip–flop mode of buckle propagation. Once initiated, a buckle localizes. Contact between the walls of the collapsing cross-section of the tube arrests local collapse and the buckle then propagates along the length of the tube. A finite time interval is required for the buckle to reach steady-state propagation. As it accelerates to steady-state, its front sharpens and, in the process, causes an increase in the reverse ovality downstream of it. If the pressure is at a high enough level, the reverse ovality eventually initiates a buckle at a new site. The new mode of collapse is at 90° to the original one. Subsequently, the events are repeated with the flipping being repeated at well defined intervals. The distance between adjacent nodes of the flip–flop buckling mode was found to be reproduced well by the model. This sequence of events extracted from the numerical simulation essentially confirms the scenario inferred by Kyriakides, 20 years ago using strictly experimental observations and intuition.

Appendix A. Outline of dynamic finite element formulation

For the dynamic problem the overall equations of motion correspond to adding a d'Alembert force to the principle of virtual work (no body forces) as follows:

$$\int_V \underline{\sigma} \cdot \delta\underline{\varepsilon}\, \mathrm{d}V = \int_V \underline{T} \cdot \delta\underline{u}\, \mathrm{d}S - \int_V \rho\underline{\ddot{u}} \cdot \delta\underline{u}\, \mathrm{d}V, \tag{A.1}$$

where $\underline{T}$ is the traction per unit current surface area (in this case, the external pressure), ρ is the current density of the material and $\underline{u}(\underline{x}, t)$ is the displacement field vector (ABAQUS, 1995). The finite element approximation to the equations of motion can be expressed as

$$\underline{M}\ddot{u} + \underline{F}_I - \underline{F}_E = \underline{0}, \tag{A.2}$$

where $\underline{M}$ is the mass matrix, $\underline{F}_I$ is the internal force vector, and $\underline{F}_E$ is the external force vector.

The equations of motion are integrated in time by using the implicit operator of Hilber et al. (1977) and Hilber and Hughes (1978). Knowing the solution at time t, the problem unknowns are solved at time $(t + \Delta t)$ based not only on values at t but also on values estimated for $(t + \Delta t)$. This is a single parameter $(-1/3 \leqslant \alpha \leqslant 0)$ operator with controllable numerical damping. If $\alpha = 0$, there is no damping, and the operator is the trapezoidal rule; if $\alpha = -1/3$, significant damping is available. The operator replaces the

actual equations of motion with a balance of d'Alambert forces at the end of the time step and a weighted average of the static forces at the beginning and end of the time step as follows:

$$\underline{M\ddot{u}}|_{t+\Delta t} + (1+\alpha)(\underline{F}_{\mathrm{I}}|_{t+\Delta t} - \underline{F}_{\mathrm{E}}|_{t+\Delta t}) - \alpha(\underline{F}_{\mathrm{I}}|_{t} - \underline{F}_{\mathrm{E}}|_{t}) = \underline{0}, \tag{A.3}$$

where

$$\underline{u}|_{t+\Delta t} = \underline{u}|_t + \Delta t\underline{\dot{u}}|_t + (\Delta t)^2[(\tfrac{1}{2}-\beta)\underline{\ddot{u}}|_t + \beta\underline{\ddot{u}}|_{t+\Delta t}],$$

$$\underline{\dot{u}}|_{t+\Delta t} = \underline{\dot{u}}|_t + \Delta t[(1-\gamma)\underline{\ddot{u}}|_t + \gamma\underline{\ddot{u}}|_{t+\Delta t}],$$

$$\beta = \tfrac{1}{4}(1-\alpha)^2 \quad \text{and} \quad \gamma = \tfrac{1}{2} - \alpha.$$

The parameter α was chosen to be -0.05, providing modest numerical damping which quickly removes any undesirable high frequency numerical noise without affecting significantly the actual response. The resulting set of nonlinear equations is then solved iteratively using Newton's method.

References

ABAQUS Theory Manual, 1995. Version 5.5, p. 2.4.1.

Chater, E., Hutchinson, J.W., 1984. On the propagation of bulges and buckles. ASME J. Appl. Mech. 51, 269–277.

Corona, E., Kyriakides, S., 1988. On the collapse of inelastic tubes under combined bending and pressure. Int. J. Solids Struct. 24, 505–535.

Dyau, J.-Y., Kyriakides, S., 1993a. On the localization of collapse in cylindrical shells under external pressure. Int. J. Solids Struct. 30, 463–482.

Dyau, J.-Y., Kyriakides, S., 1993b. On the propagation pressure of long cylindrical shells under external pressure. Int. J. Mech. Sci. 35, 675–713.

Hilber, H.M., Hughes, T.J.R., Taylor, R.L., 1977. Improved numerical dissipation for time integration algorithms in structural dynamics. Earthquake Engng. Struct. Dynam. 5, 283–292.

Hilber, H.M., Hughes, T.J.R., 1978. Collocation, dissipation and "overshoot" for time integration schemes in structural dynamics. Earthquake Engng. Struct. Dynam. 6, 99–117.

Johns, T.G., Mesloh, R.E., Winegardner, R., Sorenson, J.E., 1975. Inelastic buckling of pipelines under combined loads. Proc. Offshore Technol Conf. Houston TX, OTC Paper 2209, Vol. II, 635–646.

Ju, G.T., Kyriakides, S., 1991. Bifurcation buckling versus limit load instabilities of elastic-plastic tubes under bending and external pressure. ASME J. Offshore Mech. Arctic Engng. 113, 43–52.

Kyriakides, S., 1980. On the propagating buckle and its arrest. Ph.D. dissertation. GALCIT, California Institute of Technology, 1980.

Kyriakides, S., 1993. Propagating instabilities in structures. In: Hutchinson, J.W., Wu, T.Y. (Eds.), Adv. Appl. Mech. vol. 30, Academic Press, Boston, pp. 67–189.

Kyriakides, S., Babcock, C.D., 1979. On the dynamics and the arrest of the propagating buckle in offshore pipelines. Proc. Offshore Technol Conf, Houston TX, OTC Paper 3479, 1035–1045.

Kyriakides, S., Babcock, C.D., 1980. On the "slip-on" buckle arrestor for offshore pipelines. ASME J. Pressure Vessel Technol. 102, 188–193.

Kyriakides, S., Babcock, C.D., 1981. Experimental determination of the propagation pressure of circular pipes. ASME J. Energy Res. Technol. 104, 328–336.

Kyriakides, S., Babcock, C.D., Elyada, D., 1984a. Initiation of propagating buckles from local pipeline damages. ASME J. Energy Res. Technol. 106, 79–87.

Kyriakides, S., Yeh, M.K., Roach, D., 1984b. On the determination of the propagation pressure of long circular tubes. ASME J. Pressure Vessel Technol. 106, 150–159.

Malvern, L.E., 1951. The propagation of longitudinal waves of plastic deformation in a bar of material exhibiting a strain-rate effect. ASME J. Appl. Mech. 18, 203–208.

Murphey, C.E., Langner, C.G., 1985. Ultimate pipe strength under bending, collapse and fatigue. Proc. Fourth Int. Conf. Offshore Mech. Arctic Engng. 1, 467–477.

Netto, T.A., 1998. On the dynamics and arrest of propagating buckles in offshore pipelines. Ph.D. Dissertation, Engineering Mechanics, The University of Texas at Austin, MSS&M Report No. 98/16.

Netto, T.A., Kyriakides, S., 2000a. Dynamic performance of integral buckle arrestors for offshore pipelines. Part I Exp. Int. J. Mech. Sci., in press.

Netto, T.A., Kyriakides, S., 2000b. Dynamic performance of integral buckle arrestors for offshore pipelines. Part II Analysis. Int. J. Mech. Sci., in press.

Netto, T.A., Kyriakides, S., Ouyang, X., 1998. On the initiation and propagation of buckles on a beam on a nonlinear foundation. ASME J. Appl. Mech. 66, 418–426.

Park, T.-D., Kyriakides, S., 1996. On the collapse of dented cylinders under external pressure. Int. J. Mech. Sci. 38, 557–578.

Peirce, S.D., Shih, C.F., Needleman, A., 1984. A tangent modulus method for rate dependent solids. Comput. Struct. 18, 875–887.

Reid, S.R., Johnson, W., Watson, A.R., 1976. Large deformations of thin-walled tubes under transverse loading: I, II and III. Int. J. Mech. Sci. 18, pp. 325, 387, and 501.

Ripperger, E.A., 1965. Dynamic plastic behavior of aluminum, copper, and iron. In: Huffington Jr. N.J. (Ed.), Behavior of Materials Under Dynamic Loading. ASME, 62–80.

Song, H.-W., Tassoulas, J.L., 1993. Finite element analysis of propagating buckles. Int. J. Numer. Meth. Engng. 36, 3529–3552.

Yuan, S.W., 1946. Thin cylindrical shells subjected to concentrated loads. Quart. Appl. Math. 4, 13–26.

Yuan, S.W., Ting, L., 1957. On radial deflections of a cylinder subjected to equal and opposite concentrated radial loads. Trans. ASME 79 and J. Appl. Mech. 24, 278–282.